Supplementary Information
Controlling Umklapp scattering in bilayer graphene moiré superlattice

Mohit Kumar Jat[1], Shubhankar Mishra[1], Harsimran Kaur Mann[1], Robin Bajaj[1], Kenji Watanabe[2], Takashi Taniguchi[3], H. R. Krishnamurthy[1], Manish Jain[11] and Aveek Bid[11,*]

[11]*Department of Physics, Indian Institute of Science, Bangalore 560012, India*
[2] *Research Center for Electronic and Optical Materials, National Institute for Materials Science, 1-1 Namiki, Tsukuba 305-0044, Japan*
[3] *Research Center for Materials Nanoarchitectonics, National Institute for Materials Science, 1-1 Namiki, Tsukuba 305-0044, Japan*

CONTENTS

S1. DEVICE FABRICATION

The hBN encapsulated bilayer graphene (BLG) devices were fabricated using the dry transfer technique [1–3]. Initially, BLG and hBN flakes were mechanically exfoliated onto a Si/SiO_2 substrate. BLG flakes were first identified with optical contrast and later confirmed with Raman spectra (Fig. S1). hBN flakes of thickness ranging from $25 - 30$ nm were used in fabrication, and their thickness uniformity was confirmed using an AFM.

To make BLG-hBN single-moiré devices (labeled M1, M2, M3 and M4), the top hBN sharp edge was aligned with the sharp edge of BLG at nearly zero degrees, facilitating a moiré between BLG and the top hBN layer. The bottom hBN edge was intentionally misaligned with BLG to prevent any moiré superlattice formation between BLG and the bottom hBN layer.

In the case of a non-moiré device (N1), hBN was misaligned with both the bottom hBN and top hBN layers to prevent any moiré superlattice formation. Electrical contacts were patterned through lithography, etched with a mixture of CHF_3 (40 sscm) and O_2 (10 sscm), and contacts deposited with Cr/Pd/Au with thickness $5/12/55$ nm to form 1D contact with BLG. The device was etched in Hall bar geometry. Finally, The top gate was patterned through lithography, and a metal gate was deposited. Having dual gates in the devices gives control in tuning the system's carrier density and displacement field independently.

S2. TWIST ANGLE ESTIMATION

Fig. S2 shows the plot of longitudinal resistance R_{xx} versus carrier density n for devices M1, M2, M3 and M4 measured for different pairs of voltage leads at $T = 2$ K. The resistance peak at $n = 0$ originates from the charge neutrality point of the BLG. The resistance peak at $n_{M1} = -2.30 \times 10^{16}$ m^{-2}, $n_{M2} = -2.49 \times 10^{16}$ m^{-2}, $n_{M3} = -2.80 \times 10^{16}$ m^{-2} and $n_{M4} = -9.07 \times 10^{16}$ m^{-2}, for device M1, M2, M3 and M4, respectively, is a consequence of all levels up to the moiré gap getting filled at this carrier density. The independence of the carrier density at which the moiré gap emerges, regardless of the

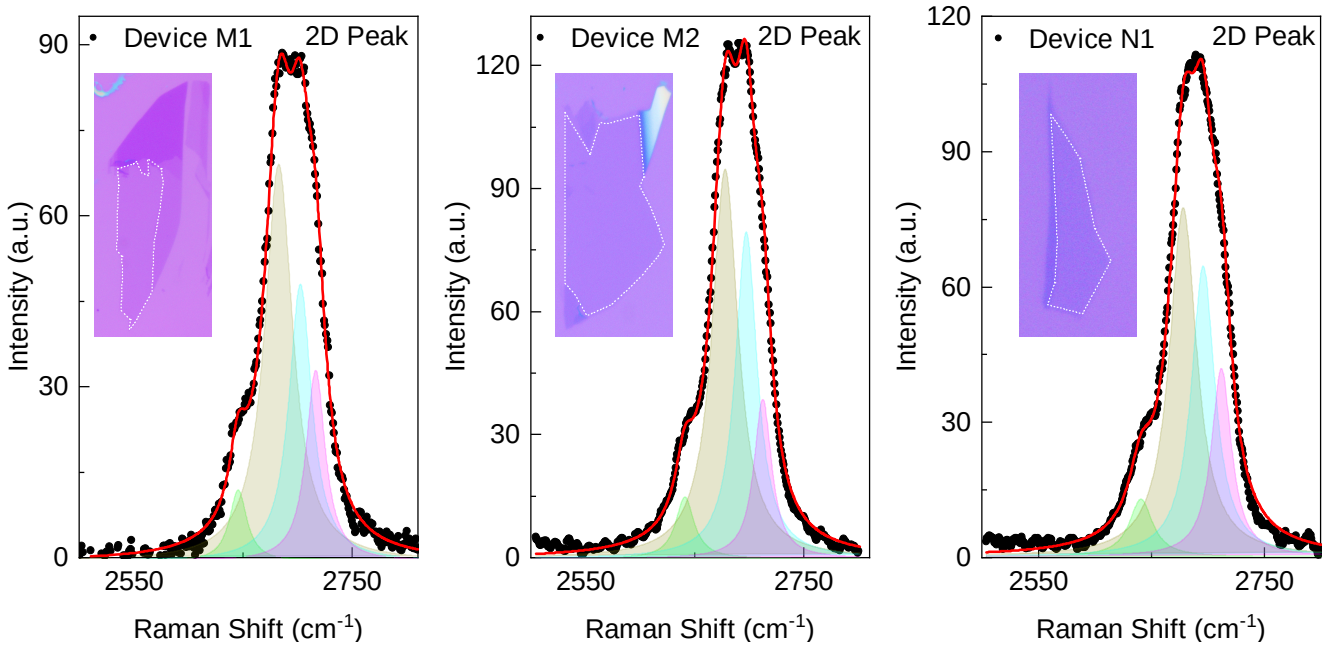

Figure S1. **Raman spectra of BLG flakes**. Plots of the 2D Raman peak of the bilayer graphene used to fabricate devices (a) M1, (b) M2, and (c) N1. The black-filled circles are the experimentally measured Raman spectra. The red solid line is cumulative of the four Lorentzian fitted to it; the four Lorentzian are also individually shown. The insets show the optical images of the BLG flakes; the shaded region marks the bilayer graphene used in device fabrication.

voltage probes used for the measurements (indicated with dotted lines), confirms the angle homogeneity in the devices. Further, Fig. S2(e) also illustrates that the carrier density corresponding to the moiré gap is independent of the applied displacement field.

The moiré wavelength is estimated using the relation [4–6]:

$$\lambda^2 = \frac{8}{\sqrt{3} n_M} \tag{S1}$$

We find $\lambda_1 = 14$ nm for device M1, $\lambda_2 = 13.64$ nm for device M2, $\lambda_3 = 12.73$ nm for device M3 and $\lambda_4 = 7.20$ nm for device M4.

We rule out dual-alignment of the BLG with both top - and bottom-hBN [5, 7] through measurements of the Brown-Zak oscillations of conductance at $T = 100$ K. At these elevated temperatures, landau levels get smeared out, and only the magnetotransport oscillations from the recurring Bloch states in the superlattice survive, and are shown in Fig.1(e) of the main text for device M1 and in Fig. S3(a,b) for device M2, M3. The periodicity of these oscillations is independent of the carrier density. The fast Fourier transform of these oscillations yields a single "frequency" $B_f = 24.2$ T, 25.7 T and 29.5 T for device M1, M2 and M3 respectively, limiting the possibility of supermoiré in the system. We note that a single Brown-Zak oscillation frequency can also occur if the two twist angles between the top hBN and BLG and that between the BLG and bottom hBN are identical; given that we intentionally misaligned the bottom hBN by a large angle, we rule out this scenario.

The frequency B_f is related to the real-space area S of the moiré unit cell by $B_f = \phi_0/S$, where $\phi_0 = h/e$ is the flux quantum [4, 8–10]. Using the relation $\lambda = \sqrt{(2S/\sqrt{3})}$, we estimate $\lambda_1 = 14$ nm (for device M1), $\lambda_2 = 13.64$ nm (for device M2) and $\lambda_3 = 12.73$ nm (for device M3). These values match exactly with the moiré wavelength extracted from resistance versus carrier density response.

We estimate the twist angle magnitude between BLG and hBN using the relation [11, 12]:

$$\lambda = \frac{(1+\epsilon)\mathrm{a}}{[\epsilon^2 + 2(1+\epsilon)(1-\cos(\theta))]^{1/2}} \tag{S2}$$

Here $\mathrm{a} = 0.246$ nm is the lattice constant of graphene, $\epsilon = 0.018$ is the lattice mismatch between the hBN and graphene,

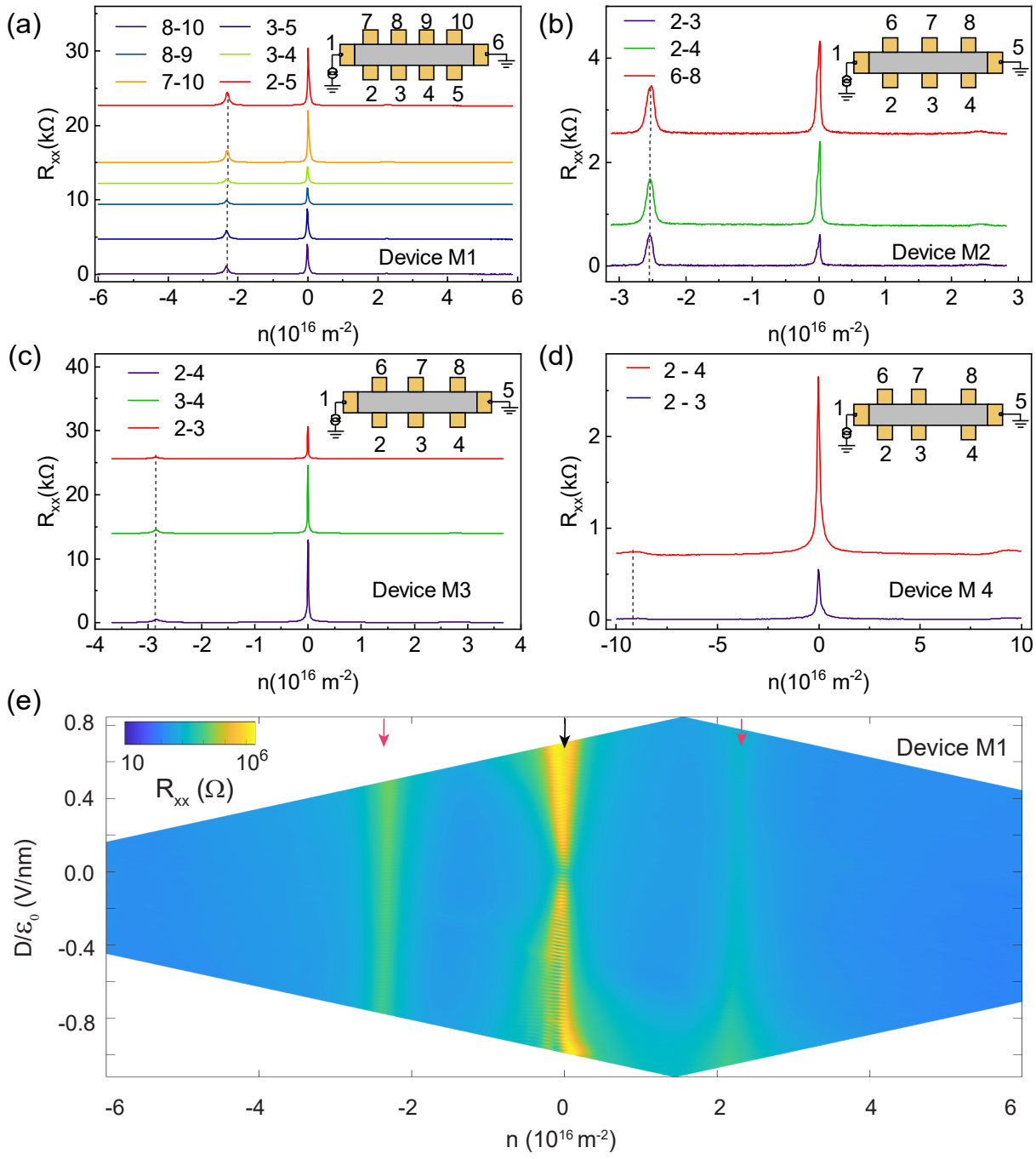

Figure S2. **Twist angle homogeneity of the moiré device.** (a) Plot of longitudinal resistance R_{xx} as a function of carrier density n measured at $T = 2$ K for several configuration for device M1. The vertical dashed line marks the carrier density at which the secondary moiré gap emerges. The current was sourced between contacts 1 and 6. The numbers in the legend are the pairs of contacts used as voltage probes for the 4-probe measurement. [(b),(c),(d)] Same as in (a) for the devices M2, M3, and M4, respectively. For four devices, the carrier density of the secondary moiré gap remains consistent across different configurations, illustrating the angle homogeneity within the devices. The plots are vertically offset for clarity. (e) 2D Plot of R_{xx} in the carrier density and the electric field D/ϵ_0 plane. The magenta (black) arrows mark the position of the moiré gap (CNP), illustrating that the position of the moiré gaps is independent of the applied perpendicular electric field.

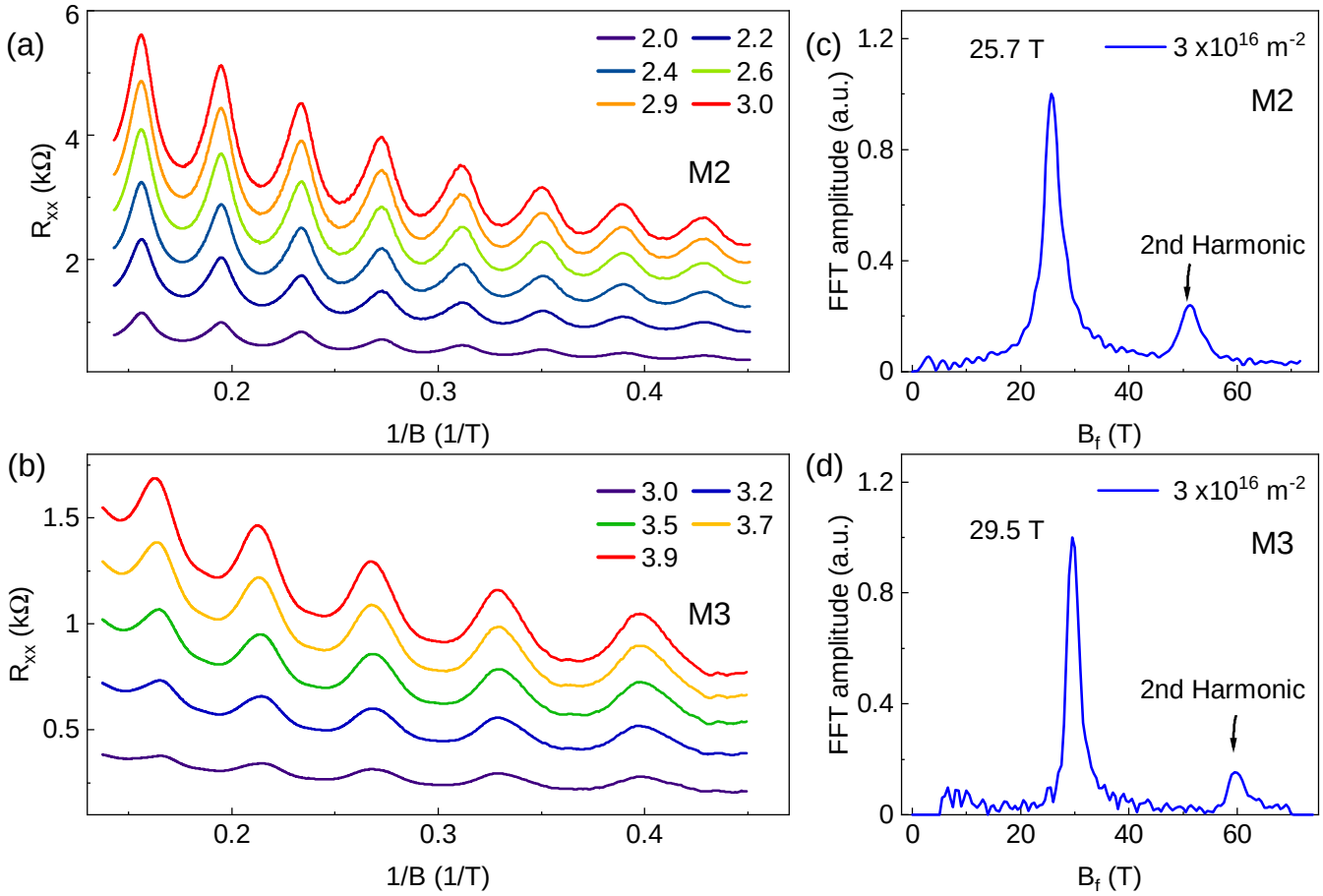

Figure S3. **Brown-Zak Oscillations of the moiré device M2 and M3 .** (a) Plot of Brown-Zak oscillations R_{xx} versus $1/B$ at a few representative values of n measured at $T = 100$ K, for device M2. The legends in the plot indicate the carrier density in units of 10^{16} m^{-2}. The data are vertically offset for clarity. (b) Same as in (a) for device M3. (c) The Fourier spectrum of the Brown-Zak oscillations measured at $n = 3 \times 10^{16}$ m^{-2}, for device M2. The peak at 25.7 T corresponds to moiré wavelength of 13.64 nm. (d) Same as in (c) for device M3, the peak at 29.5 T corresponds to moiré wavelength of 12.73 nm.

and θ is the relative twist angle between hBN and BLG. We find the twist angle between the BLG and hBN to be $\theta_{M1} = 0°$, $\theta_{M2} = 0.26°$, $\theta_{M3} = 0.47°$ and $\theta_{M4} = 1.70°$ for device M1, M2, M3 and M4, respectively.

S3. COMPARISON OF SHEET RESISTANCE BETWEEN MOIRÉ AND NON MOIRÉ DEVICE

Fig. S4(a) shows the longitudinal sheet resistance versus carrier density response for device M2 over a range of temperatures. The Umklapp electron-electron scattering dominated region is marked with dotted rectangles. The hole side (marked with an orange rectangle) shows a significantly larger strength of umklapp strength than the electron side (marked with a black rectangle). Fig.S4(b) plots the sheet resistance versus T^2 to better show this electron-hole asymmetry over a range of n/n_0. The dotted orange (black) line shows a guiding straight line for holes (electrons) type carriers. This large asymmetric strength origin can be attributed to the much larger probability of the back-scattering of holes than that of electrons [13].

The T-dependence of the sheet resistance in non-aligned device N1 are plotted in Fig. S4(c) for comparison. The data in the non-aligned device differ from that of M1 and M2 in three important aspects:

1. The large increase in sheet resistance seen in M1 and M2 with increasing T is conspicuously absent in the non-aligned device N1.

2. A T^2-dependence of the sheet resistance is not observed for the device N1 (Fig.2(d) of the main manuscript). This is expected since, in a non-aligned device, Umklapp scattering is forbidden [14].

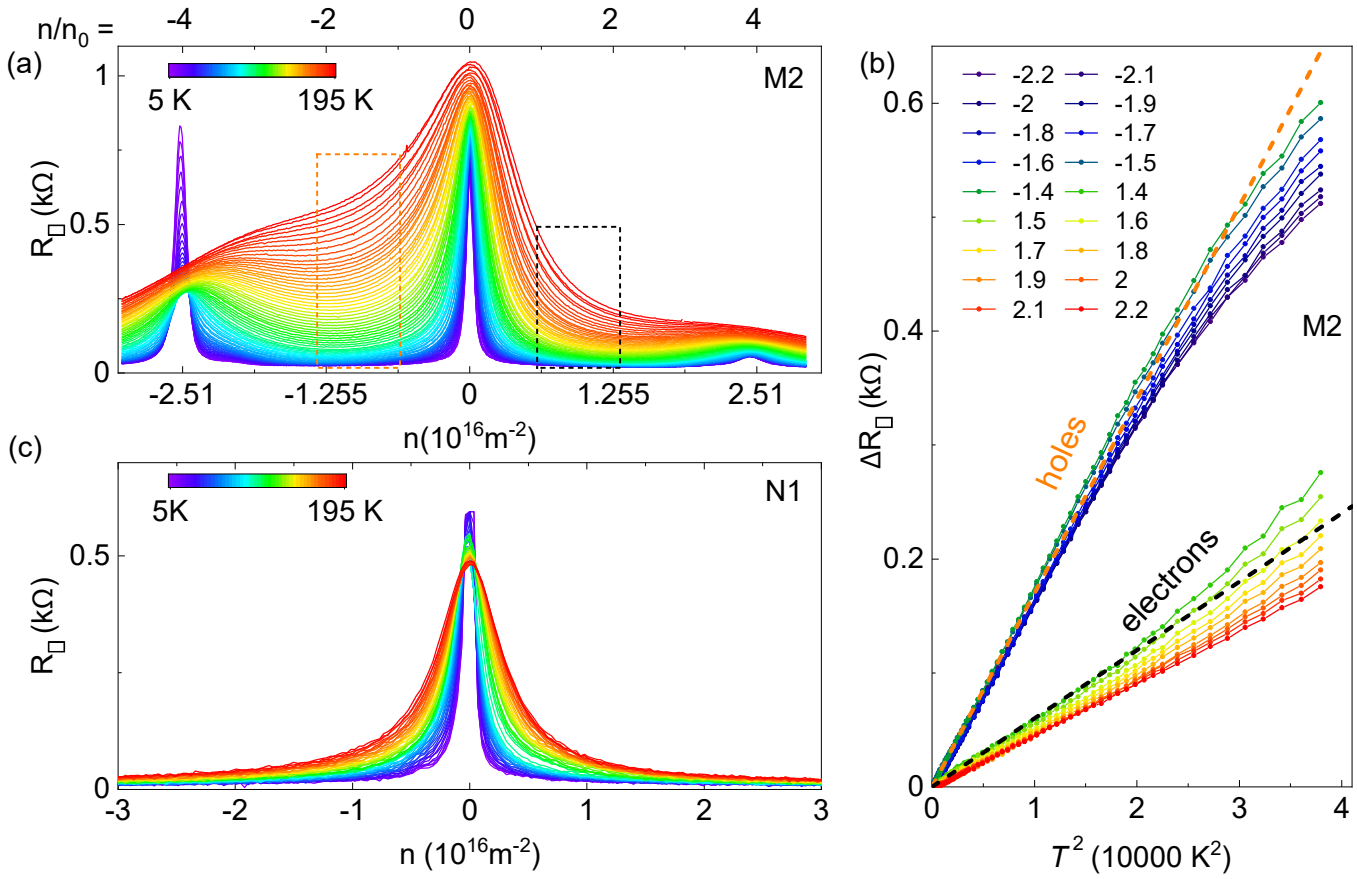

Figure S4. **Electron-Hole asymmetry of the moiré device and comparison with non-moiré device.** (a) Plot of longitudinal sheet resistance $R_\square$ as a function of filling fraction n/n_0 over a range of T from 5 K (blue) to 195 K (red). The measurements were done with $B = 0$ and $D = 0$. The dotted rectangles mark the regions where Umklapp is the dominant scattering mechanism. The plot illustrates the particle-hole asymmetry in the strength of Uee. (b) Plots of $\Delta R_\square$ versus T^2 at a few representative filling fractions (n/n_0) for electron and hole doping. The numbers in the legend are the values of n/n_0. The dotted lines are linear fits to the data at $n/n_0 = \pm 1.4$. (c) T-dependence of $R_\square$ for the non-aligned device N1 – note the absence of the large resistance enhancement with T, as seen in the case of the moiré devices.

3. In contrast to that of M1 and M2, the electron-hole asymmetry in sheet resistance is absent for device N1.

S4. CALCULATION OF THRESHOLD DENSITY

The real-space lattice of bilayer graphene and hBN leads to a hexagonal moiré lattice (Fig. S5(a)). The lattice vectors can be written as:

$$\lambda_\alpha = \frac{\lambda}{2}(\sqrt{3}, 1), \qquad \lambda_\beta = \frac{\lambda}{2}(\sqrt{3}, -1). \tag{S3}$$

where λ is the moiré wavelength. The corresponding reciprocal lattice vectors are given by (Fig.S5(b)):

$$\mathbf{G}_\alpha = \frac{2\pi}{\sqrt{3}\lambda}(1, \sqrt{3}), \qquad \mathbf{G}_\beta = \frac{2\pi}{\sqrt{3}\lambda}(1, -\sqrt{3}). \tag{S4}$$

In the Uee scattering process, the condition for backscattering is

$$\mathbf{k_1} + \mathbf{k_2} = \mathbf{k_3} + \mathbf{k_4} + \mathbf{G} \tag{S5}$$

here, $\mathbf{k_1}, \mathbf{k_2}$ are the wave-vectors of the incoming electrons, $\mathbf{k_3}, \mathbf{k_4}$ are the wave-vectors of the scattered electrons and $\mathbf{G}$ is a reciprocal space lattice vector.

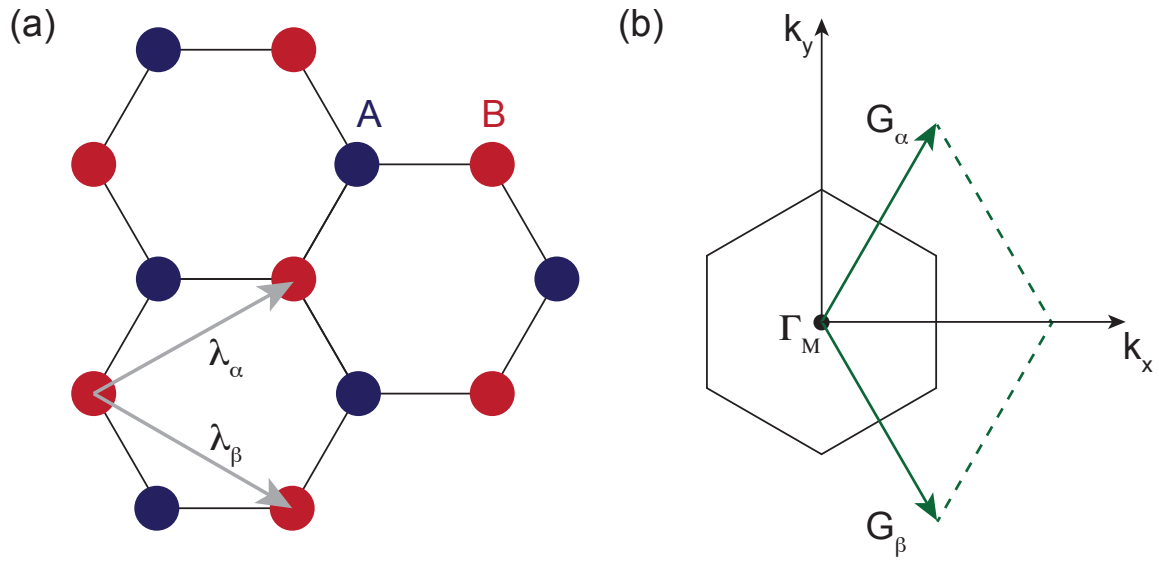

Figure S5. **Moiré lattice and its Brillouin zone.** (a) Real space lattice of the moiré lattice, λ_α and λ_β are lattice unit vectors. (b) Brillouin zone with reciprocal lattice vectors $\mathbf{G}_\alpha$ and $\mathbf{G}_\beta$.

The lower limit on wave-vector k_t above which umklapp scattering is allowed comes from Eqn. S5, which gives $k_t = G/4 = \pi/(\sqrt{3}\lambda)$. The corresponding threshold carrier density above which Umklapp scattering starts can be written as $n_t = |\mathbf{k_t}|^2/\pi = \pi/(3\lambda^2) = n_0\pi/(2\sqrt{3}) \approx 0.907 n_0$. (assuming an isotropic dispersion). Here, $n_0 = 2/(\sqrt{3}\lambda^2)$ is the carrier density corresponding to one-fourth filling of moiré band.

S5. QUANTUM HALL OF THE DEVICE

The Quantum Hall measurements at a perpendicular magnetic field of $B = 5$ T were performed to estimate the value of capacitance C_{bg} and C_{tg}. Fig.S6 shows G_{xx} (green solid line) and G_{xy} (red solid line) versus the filling fraction ($\nu = nh/eB$) measured at a perpendicular magnetic field of 5 T, establishing that both spin and valley degeneracies are lifted, indicating the high quality of the device.

S6. COMPARISION OF UMKLAPP STRENGTH IN THE HBN MOIRÉ OF BLG AND SLG

Fig.S7 plots the f_n versus moiré wavelength for the hBN moiré devices, measured at $n/n_0 = -2$. The Red data points are from our measured BLG-hBN moiré devices, and the blue data points of the SLG-hBN moiré devices from Ref [13]. As a similarity, both systems show the Umklapp scattering at $n/n_0 = -2$.

However, there are significant differences between these two material systems (Fig.S7):

1. The strength of f_n is larger in BLG-hBN moiré than in the SLG-hBN moiré.
2. f_n depends non-monotonically on the moiré wavelength for BLG-hBN moiré, whereas for SLG-hBN moiré, f_n increases monotonically with the moiré wavelength.

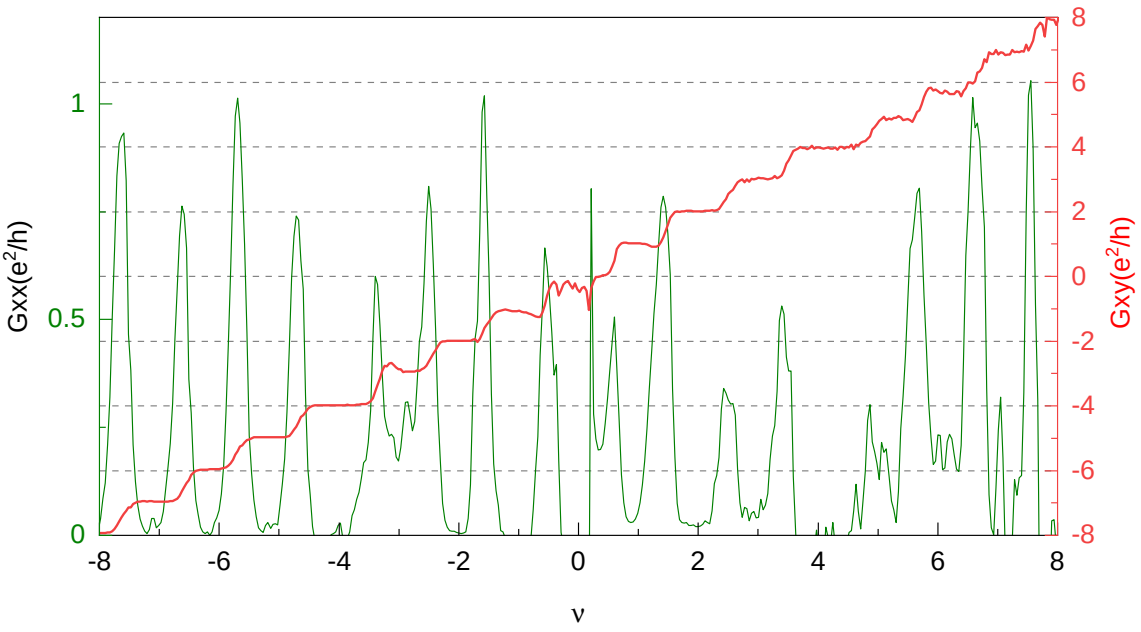

Figure S6. **Quantum Hall of the device.** Plots of G_{xx} (green solid line) and G_{xy} (red solid line) versus the filling factor $\nu = nh/eB$. The measurements were done for $B = 5$ T and at $T = 20$ mK.

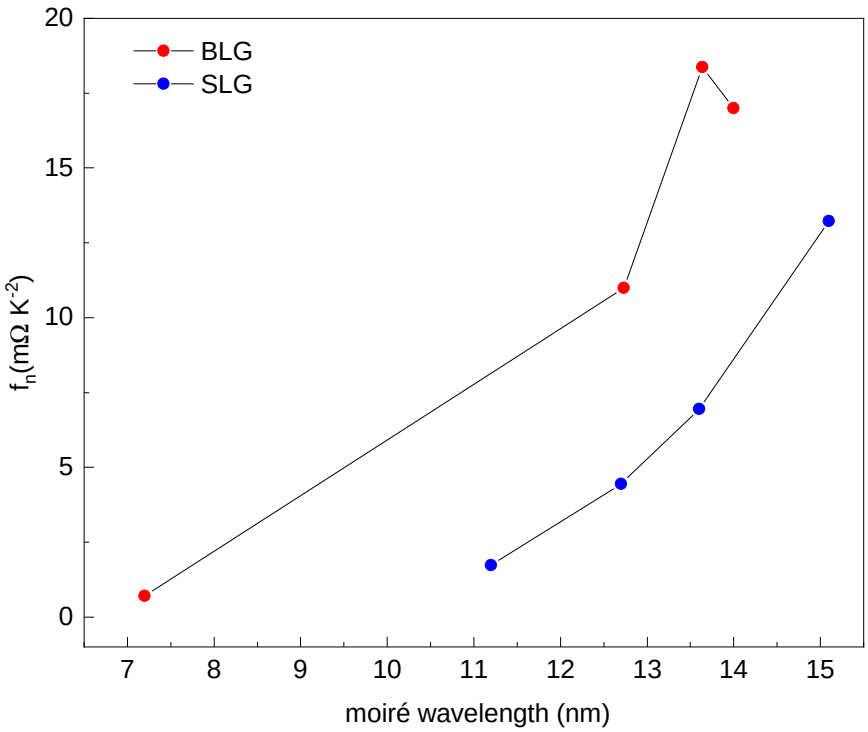

Figure S7. **Umklapp strength in the hBN moiré of BLG and SLG.** Plot of f_n versus moiré wavelength, measured at $n/n_0 = -2$. Red data points are from our measured BLG-hBN moiré devices, and blue data points are of the SLG-hBN moiré devices taken from Ref [13]

.

* aveek@iisc.ac.in

[1] P. Tiwari, D. Sahani, A. Chakraborty, K. Das, K. Watanabe, T. Taniguchi, A. Agarwal, and A. Bid, Observation of the time-reversal symmetric hall effect in graphene–wse2 heterostructures at room temperature, Nano Letters **23**, 6792 (2023).

[2] K. R. Amin, R. Nagarajan, R. Pandit, and A. Bid, Multifractal conductance fluctuations in high-mobility graphene in the integer quantum hall regime, Phys. Rev. Lett. **129**, 186802 (2022).

[3] P. Tiwari, M. K. Jat, A. Udupa, D. S. Narang, K. Watanabe, T. Taniguchi, D. Sen, and A. Bid, Experimental observation of spin-split energy dispersion in high-mobility single-layer graphene/wse2 heterostructures, npj 2D Materials and Applications **6**, 68 (2022).

[4] Y. Yang, J. Li, J. Yin, S. Xu, C. Mullan, T. Taniguchi, K. Watanabe, A. K. Geim, K. S. Novoselov, and A. Mishchenko, In situ manipulation of van der waals heterostructures for twistronics, Science Advances **6**, eabd3655 (2020).

[5] M. K. Jat, P. Tiwari, R. Bajaj, I. Shitut, S. Mandal, K. Watanabe, T. Taniguchi, H. R. Krishnamurthy, M. Jain, and A. Bid, Higher-order bragg gaps in the electronic band structure of bilayer graphene renormalized by recursive supermoiré potential. *arXiv*, 2023. arxiv:2304.01720 [cond-mat.mes-hall]. https://arxiv.org/abs/2304.01720. (accessed 2023-02-03).

[6] X. Sun, S. Zhang, Z. Liu, H. Zhu, J. Huang, K. Yuan, Z. Wang, K. Watanabe, T. Taniguchi, X. Li, M. Zhu, J. Mao, T. Yang, J. Kang, J. Liu, Y. Ye, Z. V. Han, and Z. Zhang, Correlated states in doubly-aligned hbn/graphene/hbn heterostructures, Nature Communications **12**, 7196 (2021).

[7] Z. Wang, Y. B. Wang, J. Yin, E. Tóvári, Y. Yang, L. Lin, M. Holwill, J. Birkbeck, D. J. Perello, S. Xu, J. Zultak, R. V. Gorbachev, A. V. Kretinin, T. Taniguchi, K. Watanabe, S. V. Morozov, M. Anđelković, S. P. Milovanović, L. Covaci, F. M. Peeters, A. Mishchenko, A. K. Geim, K. S. Novoselov, V. I. Falko, A. Knothe, and C. R. Woods, Composite super-moiré; lattices in double-aligned graphene heterostructures, Science Advances **5**, eaay8897 (2019).

[8] D. R. Hofstadter, Energy levels and wave functions of bloch electrons in rational and irrational magnetic fields, Phys. Rev. B **14**, 2239 (1976).

[9] R. Huber, M.-N. Steffen, M. Drienovsky, A. Sandner, K. Watanabe, T. Taniguchi, D. Pfannkuche, D. Weiss, and J. Eroms, Band conductivity oscillations in a gate-tunable graphene superlattice, Nature Communications **13**, 2856 (2022).

[10] R. K. Kumar, X. Chen, G. H. Auton, A. Mishchenko, D. A. Bandurin, S. V. Morozov, Y. Cao, E. Khestanova, M. B. Shalom, A. V. Kretinin, K. S. Novoselov, L. Eaves, I. V. Grigorieva, L. A. Ponomarenko, V. I. Fal'ko, and A. K. Geim, High-temperature quantum oscillations caused by recurring bloch states in graphene superlattices, Science **357**, 181 (2017).

[11] B. Hunt, J. D. Sanchez-Yamagishi, A. F. Young, M. Yankowitz, B. J. LeRoy, K. Watanabe, T. Taniguchi, P. Moon, M. Koshino, P. Jarillo-Herrero, and R. C. Ashoori, Massive dirac fermions and hofstadter butterfly in a van der waals heterostructure, Science **340**, 1427 (2013).

[12] L. Wang, S. Zihlmann, M.-H. Liu, P. Makk, K. Watanabe, T. Taniguchi, A. Baumgartner, and C. Schönenberger, New generation of moiré superlattices in doubly aligned hbn/graphene/hbn heterostructures, Nano Letters **19**, 2371 (2019).

[13] J. R. Wallbank, R. Krishna Kumar, M. Holwill, Z. Wang, G. H. Auton, J. Birkbeck, A. Mishchenko, L. A. Ponomarenko, K. Watanabe, T. Taniguchi, K. S. Novoselov, I. L. Aleiner, A. K. Geim, and V. I. Falko, Excess resistivity in graphene superlattices caused by umklapp electron-electron scattering, Nature Physics **15**, 32 (2019).

[14] C. Moulsdale and V. Fal'ko, Umklapp electron-electron scattering in bilayer graphene moiré superlattice, Phys. Rev. B **107**, 144111 (2023).